Tidal field anisotropy as a tracer of cosmic voids

Sebastian Bustamante [*1], Jaime E. Forero-Romero[2]

[1]*Instituto de Física - FCEN, Universidad de Antioquia, Calle 67 No. 53-108, Medellín, Colombia*
[2]*Departamento de Física, Universidad de los Andes, Cra. 1 No. 18A-10, Edificio Ip, Bogotá, Colombia*

20 January 2015

ABSTRACT

Finding and characterizing underdense regions (voids) in the large scale structure of the Universe is an important task in cosmological studies. In this paper we present a novel approach to find voids in cosmological simulations. Our approach is based on algorithms that use the tidal and the velocity shear tensors to locally define the cosmic web. Voids are identified using the fractional anisotropy (FA) computed from the eigenvalues of each web scheme. We define the void boundaries using a watershed transform based on the local minima of the FA and its boundaries as the regions where the FA is maximized This void identification technique does not have any free parameters and does not make any assumption on the shape or structure of the voids. We test the method on the Bolshoi simulation and report on the density and velo ity profiles for the voids found using this new scheme.

Key words: Cosmology: theory - large-scale structure of Universe - Methods: data analysis - numerical - N-body simulations

1 INTRODUCTION

Since voids were found in the first compiled galaxy surveys they have been identified as one of the most striking features of the Cosmic Web (Chincarini & Rood 1975; Gregory & Thompson 1978; Einasto et al. 1980a,b; Kirshner et al. 1981; Zeldovich et al. 1982; Kirshner et al. 1987; Bond et al. 1996). However, due to the large volume extension of void regions ($\sim 5 - 10$ Mpch^{-1}), statistically meaningful catalogues of voids (Pan et al. 2012; Sutter et al. 2012; Nadathur & Hotchkiss 2014) have only become available through modern galaxy surveys like the two-degree field Galaxy Redshift Survey (Colless et al. 2001, 2003) and the Sloan Digital Sky Survey (York et al. 2000; Abazajian et al. 2003). This advancement generated a great interest to study voids observationally during the last decade (Hoyle & Vogeley 2004; Croton & et al. 2004; Rojas et al. 2005; Ceccarelli et al. 2006; Patiri et al. 2006; Tikhonov 2006; Patiri et al. 2006; Tikhonov 2007; von Benda-Beckmann & Müller 2008; Foster & Nelson 2009; Ceccarelli et al. 2013; Sutter et al. 2014).

On the theoretical side the rough theoretical framework that explains the origin of voids was established in the seminal work of Zel'dovich (1970) and refined in the following decades. The first detailed theoretical models describing formation, dynamics and properties of voids (Hoffman & Shaham 1982; Icke 1984; Bertschinger 1985; Blumenthal et al. 1992) were complemented and extended by numerical stud-

ies (Martel & Wasserman 1990; Regos & Geller 1991; van de Weygaert & van Kampen 1993; Dubinski et al. 1993; Bond et al. 1996). Currently, the dominant tendency to study voids relies on using data from N-body simulations. For an extensive compilation of previous numerical works we refer the reader to Colberg et al. (2008).

The relevance of voids to cosmological studies can be summarized in three aspects (Platen et al. 2007). First, voids are a key ingredient of the Cosmic Web. They dominate the volume distribution at large-scales and additionally, they compensate overdense structures in the total budget of matter. Second, voids provide a valuable resource for inferring and probing cosmological parameters as their structure and dynamics are highly determined by these values. Third, they are a largely a largely pristine environment to test galaxy evolution.

Although a visual recognition of voids in galaxy surveys and simulations is possible in most cases, a formal systematic identification is desirable for statistical studies. However, the community does not have an unambiguous definition of cosmic voids. There are nany different void finding techniques in the literature (for a detailed comparison of different schemes, see the Void Finder Comparison Project Colberg et al. (2008)). In spite of the diversity of existing schemes, they can be roughly classified into two main types. First, geometric schemes based on point spatial or redshift distribution of galaxies in surveys or dark matter halos in simulations (Kauffmann & Fairall 1991; Müller et al. 2000; Gottlöber et al. 2003; Hoyle & Vogeley 2004; Brunino et al.

---

* sebastian.bustamante@udea.edu.co

2007; Foster & Nelson 2009; Micheletti & et al. 2014; Sutter et al. 2014); second, schemes based on the smooth and continuous matter density field either from simulations or from reconstruction procedures on surveys (Plionis & Basilakos 2002; Colberg et al. 2005; Shandarin et al. 2006; Platen et al. 2007; Neyrinck 2008; Muñoz-Cuartas et al. 2011; Neyrinck et al. 2013; Ricciardelli et al. 2013).

Here we introduce a new tracer of the structure of cosmic voids that can be used once the continous matter density or velocity distribution is known. The algorithm is based on two tensorial schemes used to classify the cosmic web. The first (the T-web) is based on the Hessian of the gravitational potential or tidal tensor (Hahn et al. 2007; Forero-Romero et al. 2009). The second (the V-web) is based on the velocity shear tensor (Hoffman et al. 2012). These web schemes classify the Cosmic Web into four different types of environment depending on the counting of the number of eigenvalues below an user-defined threshold (λ_{rmth}): voids, sheets, filaments and knots for $3, 2, 1$ or 0 eigenvalues below λ_{th}, respectively.

This procedure allows a new description of the internal structure of voids that goes beyond a simple definition of a void as just an underdense regions in the large-scale matter distribution. The tidal and the shear tensors encode more information than the density field as they trace the collapsing or expanding nature of the matter field, which defines the dynamics of the Cosmic Web.

The tracer that we use to define the voids is the fractional anisotropy (FA) computed from the set of eigenvalues of the tensor under consideration. The FA was initially introduced by Basser (1995) to quantify the anisotropy degree of the diffusivity of water molecules through cerebral tissue in nuclear magnetic resonance imaging. Libeskind et al. (2013) introduced this concept in the context of Cosmic Web classification schemes.

Once we establish the FA as a void tracer, we proceed to identify individual voids as basins of local minima. For this we implement a *watershed transform algorithm* (Beucher & Lantuejoul 1979; Beucher & Meyer 1993) which has been used to define as catching basins of local minima of the density field (Platen et al. 2007; Neyrinck 2008); we use insted minima of the FA field to find define the voids.

This paper is organized as follows. In Section 2 we describe the algorithms we use to find the cosmic web in N-body simulations. In Section 3 we describe the used simulation. Then in Section 4 we explain in detail our void finder based on the fractional anisotropy of the tidal and shear tensor fields. Our results are presented in 5 to finally comment and conclude about these findings in Section 6.

2 ALGORITHMS TO LABEL THE COSMIC WEB

2.1 The tidal web (Tweb)

This scheme was initially proposed by Hahn et al. (2007) as an alternative for classifying the Cosmic Web based on the tidal tensor. The tidal tensor allows a classification in terms of the orbital dinamics of the matter field This approach extends to second-order the equations of motion around local minima of the gravitational potential. The second-order term corresponds to the tidal tensor, which is defined as the Hessian matrix of the normalized gravitational potential.

$$T_{\alpha\beta} = \frac{\partial^2 \phi}{\partial x_\alpha \partial x_\beta}, \tag{1}$$

where the physical gravitational potential has been rescaled by a factor of $4\pi G\bar{\rho}$ in such a way that ϕ satisfies the following Poisson equation

$$\nabla^2 \phi = \delta, \tag{2}$$

with $\bar{\rho}$ the average density in the Universe, G the gravitational constant and δ the dimensionless matter overdensity.

Since the tidal tensor can be represented by a real and symmetric 3×3 matrix, it is always possible to diagonalize it and obtain three real eigenvalues $\lambda_1 \geqslant \lambda_2 \geqslant \lambda_3$ with its corresponding eigenvectors $\mathbf{u}_1$, $\mathbf{u}_2$, $\mathbf{u}_3$. This set of eigenvalues are indicators of the local orbital stability in each direction $\mathbf{u}_i$, which is to label the Cosmic Web. The number of positive (stable) or negative (unstable) eigenvalues allows to label a location into one of the next four types of environment: voids (3 negatives eigenvalues), sheets (2), filaments (1) and knots (0). A modification to this scheme was introduced by Forero-Romero et al. (2009) by means of a relaxation of the stability criterion. The relative strength of each eigenvalue is no longer defined by the sign, but instead by a threshold value λ_{th} that can be tuned in such a way that the visual impression of the web-like matter distribution is reproduced.

2.2 The velocity web (Vweb)

We also use a kinematic scheme to define the Cosmic Web environment in the simulation, which has been thoroughly described in Hoffman et al. (2012). This scheme has been used to study the shape, spin and peculiar velocity alignments of dark matter halos with the cosmic web (Libeskind et al. 2013; Forero-Romero et al. 2014). We refer the reader to these papers to find a detailed description of the algorithm, its limitations and capabilities. The Vweb scheme for environment finding is based on the local velocity shear tensor calculated from the smoothed dark matter velocity field in the simulation. This tensor is given by the following expression

$$\Sigma_{\alpha\beta} = -\frac{1}{2H_0} \left(\frac{\partial v_\alpha}{\partial x_\beta} + \frac{\partial v_\beta}{\partial x_\alpha} \right), \tag{3}$$

where v_α and x_α represent the α component of the comoving velocity and position, respectively. Like the tidal tensor, $\Sigma_{\alpha\beta}$ can be represented by a 3×3 symmetric matrix with real values, making it possible to find three real eigenvalues and its corresponding eigenvectors.

In this case we also use the relative strength of the three eigenvalues with respect to a threshold value λ_{th} to classify the cosmic web in the four web types we have already described.

Usually, the threshold is a free parameter that is tuned to reproduce the visual appearence of the comic web. In this paper we take a different approach. We find the optimal value of the threshold based on the maximization of the

fractional anisotropy field in the locations label as filaments and walls.

3 NUMERICAL SIMULATIONS

We use the Bolshoi simulation to test the method describe in the paper. This simulation follows the non-linear evolution of a dark matter density field on a cubic volume of size $250h^{-1}$Mpc sampled with 2048^3 particles. The cosmological parameters in the simulation are $\Omega_{\mathrm{m}} = 0.27$, $\Omega_\Lambda = 0.73$, $h = 0.70$, $n = 0.95$ and $\sigma_8 = 0.82$ for the matter density, cosmological constant, dimensionless Hubble parameter, spectral index of primordial density perturbations and normalization for the power spectrum, respectively. This values are consistent with the seventh year of data of the Wilkinson Microwave Anisotropy Probe (WMAP) (Jarosik et al. 2011). For more detailed technical information about the simulation, see Klypin et al. (2011).

We find the cosmic web we estimate first the density and velocity fields using a *cloud-in-cell* (`CIC`) algorithm onto a grid of 256^3 cells, corresponding to a spatial resolution of $0.98h^{-1}$Mpc per cell side. These fields are smoothed with a gaussian filter with a width of $\sigma = 0.98h^{-1}$Mpc. We compute the tidal and shear tensors through finite-differences and Finally, the eigenvalues and eigenvectors of the tensor are obtained for each grid cell. The data we use here is publicly available through the MultiDark database `http://www.multidark.org/MultiDark/` which is described in Riebe et al. (2013).

4 A NEW VOID FINDING TECHNIQUE

4.1 The fractional anisotropy

The fractional anisotropy (FA), as developed by Basser (1995), was conceived to quantify the anisotropy degree of a diffusion process, e.g. the diffusivity of water molecules through cerebral tissue in nuclear magnetic resonance imaging. Here we propose the FA, much in the same way as Libeskind et al. (2013), as a tracer of cosmic voids.

The FA is defined as follows.

$$\text{FA} = \frac{1}{\sqrt{3}} \sqrt{\frac{(\lambda_1 - \lambda_3)^2 + (\lambda_2 - \lambda_3)^2 + (\lambda_1 - \lambda_2)^2}{\lambda_1^2 + \lambda_2^2 + \lambda_3^2}}, \quad (4)$$

where the eigenvalues are taken from either the Tweb or the Vweb (FA-Tweb and FA-Vweb respectively). Such as it is defined, FA$= 0$ corresponds to an isotropic distribution ($\lambda_1 = \lambda_2 = \lambda_3$) and FA$= 1$ with a highly anisotropic distribution.

In left panels of Fig. 1 we show the FA field for both web schemes over a slide of the simulation. From this Figure we can observe that both, voids and knots, display a highly isotropic expanding dynamic at their centres, becoming gradually more anisotropic at outer regions. On the other hand the filamentary structure is traced by high FA values. These characteristics are the key to use the FA as a tracer of cosmic voids.

4.2 Fractional anisotropy as a void tracer

Voids are regions where $\lambda_3 \leqslant \lambda_2 \leqslant \lambda_1 \leqslant \lambda_{th}$. This implies that a void is completely fixed by the relative strength of the λ_1 eigenvalue with respect to the λ_{th}. As we increase/decrease the threshold value λ_{th}, voids increase/decrease progressively through contours of increasing/decreasing λ_1.

Voids are thus characterized by low values of both FA and λ_1. In Fig. 2 we show that the these two values are indeed closely correlated. The left panel shows the correlation between λ_1 and FA for all the grid cells in the simulation while the right panel shows the correlation between λ_1 and the local overdensity δ. This shows that the overdensity has a large scatter at fixed λ_1.

From Figs. 1 and 2 we conclude that the FA is a good tracer of voids as it is almost perfectly correlated with low values of λ_1. We propose that voids should be composed completely by regions of FA< 0.95. If we increase the values of λ_1 from its minimum until it we reach FA$= 0.95$ in 2 we find that this correspond to critical values of $\lambda_1^T = 0.265$ and $\lambda_1^V = 0.175$ for the Tweb and Vweb, respectively. This means that setting λ_{th} to either $\lambda_1^T / \lambda_1^V$ automatically produces voids with all the cells $FA < 0.95$. The middle column in Fig. 1 shows the web classification for this choice of λ_{th}, demonstrating that it is a sensible choice to define voids.

## 4.3 Defining voids with a watershed algorithm

Once established the FA as a good tracer of voids, the next step is to find individuals voids in the overall distribution. For this purpose, we use the *watershed transform algorithm* (Beucher & Lantuejoul 1979; Beucher & Meyer 1993), in which a void is identified as the catching basin of a local minimum of the FA. The use of this algorithm is advantageous as it is parameter-free and does not require any assumption on the shape and morphology of voids.

Previous implementations of this technique as those of Platen et al. (2007); Neyrinck (2008) have shown remarkable results regarding voids finding, however they use the density field instead of the FA field. On the other hand, we use a *cloud-in-cell* (`CIC`) algorithm on a Cartesian mesh for estimating the density and tensor fields, instead of the more sophisticated *Delaunay tessellation for field estimator* (`DTFE`) technique (Schaap & van de Weygaert 2000), but our implementation of the watershed transform should not be significantly affected as we are interested in low density regions where the `CIC` gives similar estimations.

As suggested by Platen et al. (2007) and references therein, it is necessary to apply a threshold merger in order to reduce spurious features and to avoid void hierarchization. A natural choice is a threshold of $\delta = -0.8$, which means that any ridge between two voids with density below that value would be removed and the respective voids merged. As we are working with the FA, the equivalent threshold according to Fig. 2 is $FA = 0.65$. In right panels of Fig. 1 we show the resulting catalogues of voids for both schemes.
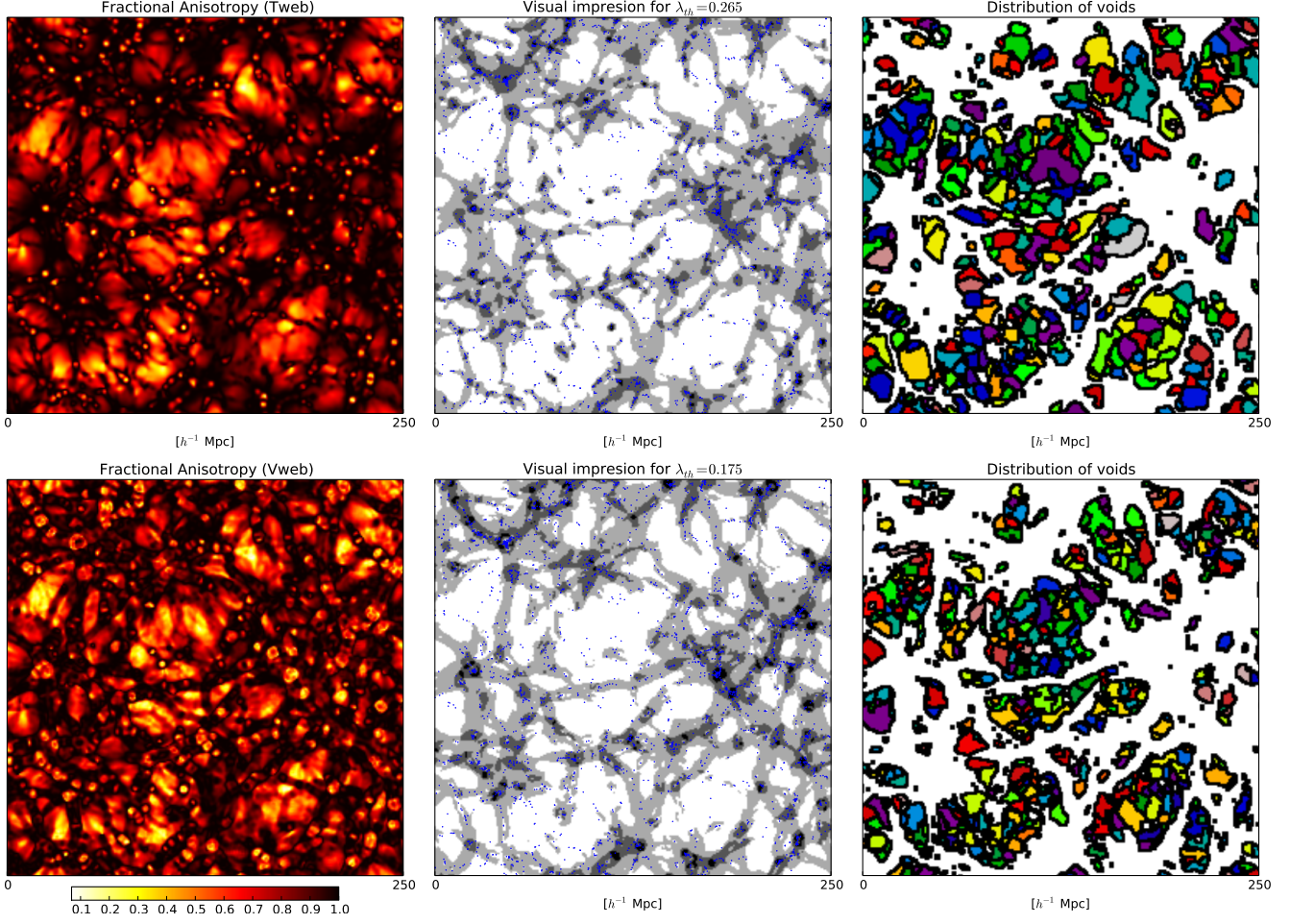
Figure 1. Left colum. Visual impression of the FA field over a slide of the simulation for each web scheme (T-web, upper panels. V-web, middle panels). Middle column. Components of the Cosmic Web using λ_{th} values that put an upper bound of $FA = 0.95$ to voids. Voids corresponds with white, sheets to gray, filaments to dark gray and knots with black regions. Right column. Sketches the distribution of the catalogued voids by our method.
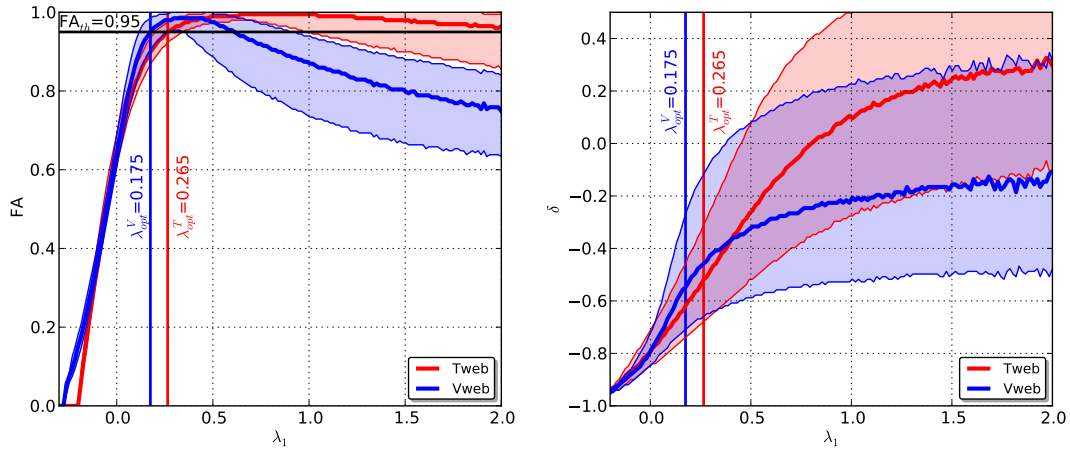
Figure 2. Distributions of the FA (left panel) and the density field (right panel) with respect to the eigenvalue λ_1 for each web scheme (Tweb, red lines. Vweb, blue lines) as calculated over all cells of the grid. Thick central lines correspond with the median and filled regions with the 50% of the distribution.
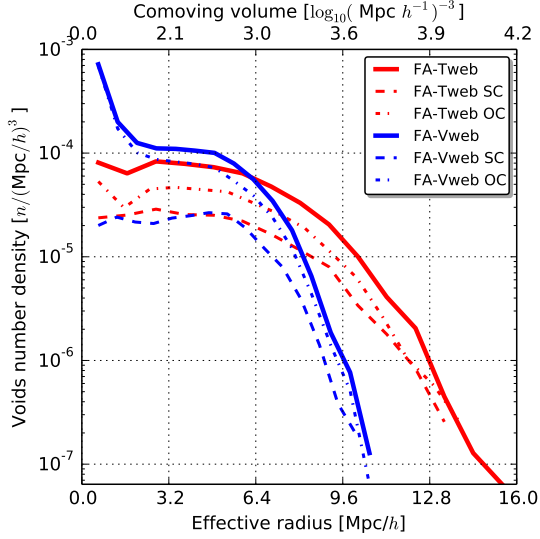
Figure 3. Volume size distribution of voids for both catalogues. FA-Tweb (red curves), FA-Vweb (blue curves). Continuous lines corresponds with the total number of voids, dot-dashed with subcompensated voids and dashed lines with over-compensated voids.

5 RESULTS

5.1 Enclosed mass

When we analyse individual density profiles of voids (see left panels of Fig. 4), they seem to be distributed in two different families, differentiated by the presence or absence of a compensation ridge (e.g. see also Fig. 14 of Colberg et al. (2005)). In order to discriminate each void in one of the families, we propose the compensation index $\mathcal{C}$, which is defined as the mass of a void enclosed in a spherical volume of radius R and normalized by the mass of the same volume as assuming the mean background density instead

$$\mathcal{C} = \frac{M_v}{\overline{M}} = \frac{3}{2R^3} \int_0^R [\delta(r) + 1] r^2 dr \qquad (5)$$

We choose an integration radius of $R = 4r_{\rm eff}$, that is large enough to enclose the compensation ridge for a typical void in case there is one. This leads us to voids with $\mathcal{C} > 1$ having more mass than expected, constituting the family of overcompensated voids. These voids generally exhibit a compensation ridge associated to dense nearby structures. In the same fashion, voids with $\mathcal{C} < 1$ constitute the family of subcompensated voids.

5.2 The void size distribution

Since the shape of the voids exhibit a wide range of geometries, a common way to represent their size is through the equivalent spherical radius or effective radius, defined as $r_{\rm eff} = [3/(4\pi)V]^{1/3}$, with V the total volume of the void. As mentioned before, we applied a threshold merger in order to avoid void hierarchization, what means we are working with the top hierarchy of voids. We limit our findings to voids with effective radius greater than the smoothing length of the density field, i.e. $\sim 1h^{-1}{\rm Mpc}$. Below that scale numerical resolution effects becomes important. We find a volume

filling fraction of voids of 54.88% of the total volume of the simulation for the FA-Tweb and 47.06% for the FA-Vweb.

In Fig. 3 we show the void size distributions for both schemes and for the overall distribution of voids as well as for overcompensated and subcompensated void subsamples. The central region of the distributions ($3h^{-1}{\rm Mpc}$ – $6h^{-1}{\rm Mpc}$), exhibit an approximately flat shape, contrary to expected from highly non-linear structures like dark matter halos, where the abundances increase for smaller structures. The distribution of the FA-Tweb is consistent with a two-barrier problem (Sheth & van de Weygaert 2004): formation of large voids is inhibited by the *void-in-void* problem (first barrier), where large voids are constituted hierarchically of smaller ones. In turn, formation of small voids is damped by the *void-in-cloud* problem (second barrier), where nearby collapsing structures limit the abundance of embedded small voids.

The FA-Vweb scheme does not tackle properly the *void-in-cloud* problem as it predicts large abundances of smaller voids. However, an interesting result is the difference between the overcompensated and subcompensated subsamples. Subcompensated voids, which are expected to be embedded in low-density regions like walls and larger voids, exhibit smaller abundances compatible with the result of the FA-Tweb. Then, the most dramatic contribution to the overabundance of small voids for the FA-Vweb comes from overcompensated voids. This implies that, although nearby non-linear structures squeeze out embedded smaller voids, the rapid and isotropic collapse in these zones, along with the more rugged nature of the velocity field make these voids still detectable by this scheme.

For both schemes overcompensated voids are more abundant, however at larger scales abundances of subcompensated voids become comparable. This is somehow expected as larger voids are more likely to abut other voids. A recent estimation of the radius of the local void gives $r_{LV} \approx 10$ Mpc (Nasonova & Karachentsev 2011). Taking the dimensionless Hubble constant as $h = 0.70$, the size of the local void would be around $r_{\rm eff} = 7\,h^{-1}{\rm Mpc}$ in the shown distribution. For both schemes, this places the local void as a rather common void in terms of size, and more likely to be overcompensated.

5.3 Physical profiles of voids

In Fig. 4 we analyse the internal properties of the found voids. We calculate the contrast density, radial-projected velocity and FA profiles. For this purpose we catalogue all the voids in several radial bins in order to capture possible size effects; moreover we show profiles for both, subcompensated and overcompensated voids. Then, for each void, we take the distance of each member cell to the void centre along with the properties of interest. Normalizing these distances with the effective radius, we stack all the voids of a radial bin in order to compute the radial profiles.

5.3.1 Density profiles

In left panels of Fig. 4 we compute density profiles of voids stacked according to their size and their compensation index. Instead of calculating the radial internal structure inside
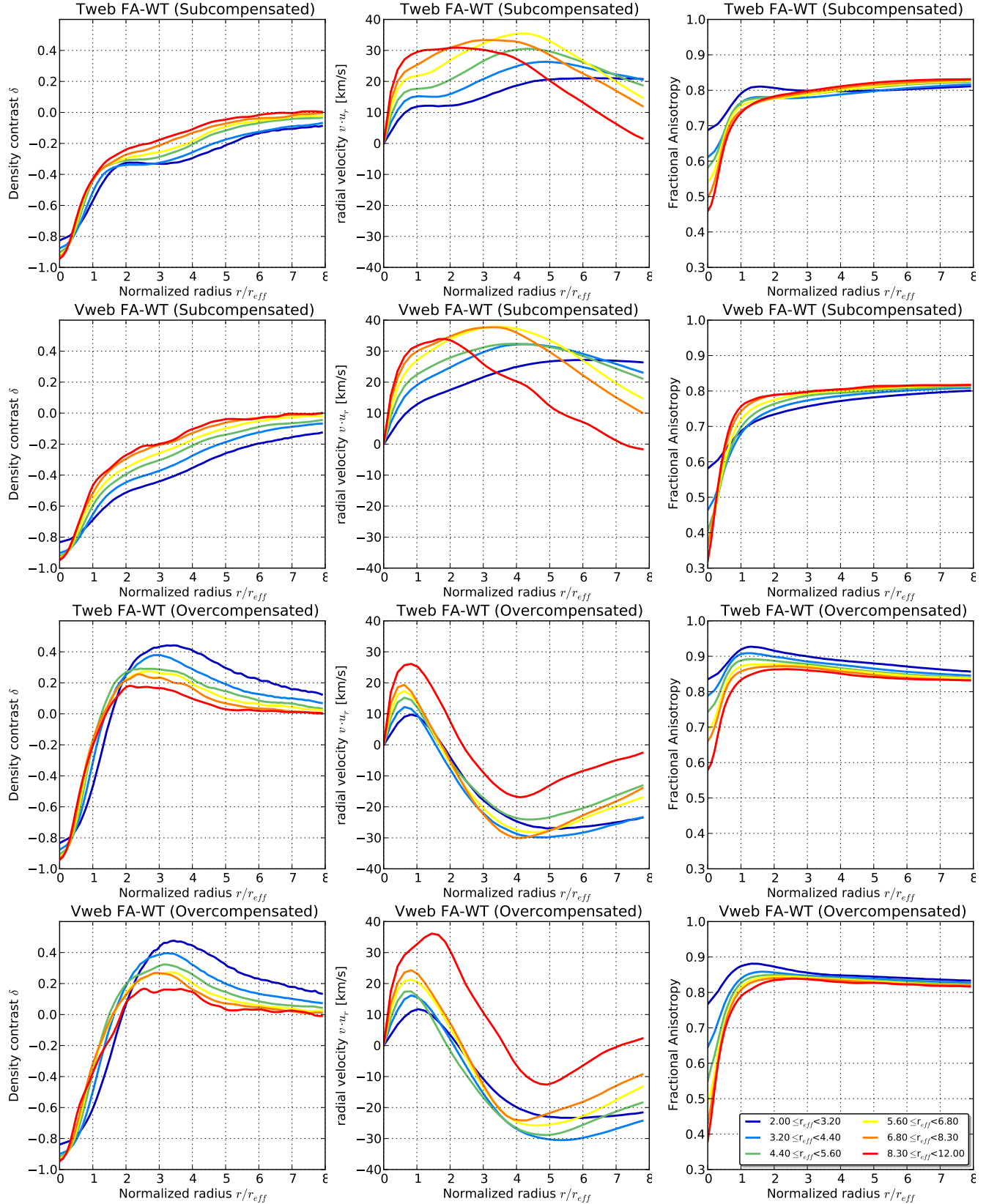
Figure 4. Physical internal properties of voids for the two finding scheme. Density field (left panels), radial-projected velocity field (middle panels) and FA field (right panels). The analysis is performed for both, subcompensated (first two rows) and overcompensated voids (last two rows).

an effective radius, we opted for a radius well beyond that value (8 r_{eff}) in order to capture the properties of neighbour structures as well.

A first interesting result is the value at the void centres: the larger the void, the more underdense their value at the centre, ranging from $\delta \approx -0.95$ for the largest voids ($8.3 - 12\ h^{-1}$Mpc) to $\delta \approx -0.8$ for the smallest voids ($2 - 3.2\ h^{-1}$Mpc). This holds for all the voids in both schemes. These very low values are consistent with most of the void finding schemes based on smooth and continuous fields from simulation or reconstruction procedures on surveys (Plionis & Basilakos 2002; Colberg et al. 2005; Shandarin et al. 2006; Platen et al. 2007; Neyrinck 2008; Muñoz-Cuartas et al. 2011; Neyrinck et al. 2013; Ricciardelli et al. 2013), unlike geometrical approaches based on point distributions, where central values are generally higher (Colberg et al. 2008).

Another important result is the steepness of the profiles at inner regions. For subcompensated voids, larger voids are more steep, reaching the mean density value at lower radius. Smaller voids exhibit moderate slopes, reaching the mean density at much larger radius. This indicates smaller subcompensated voids are embedded into low density structures like larger voids and still forming regions like walls. For subcompensated large voids, outer radial layers are so vast that all sort of structures are stacked, thus reaching the mean density at lower radius. This result remains also for overcompensated voids, where larger voids reach first both, the compensation ridge and then the mean density value.

Regarding overcompensated voids, a final result is related to the height of the compensation ridge: the larger the void size, the lower the ridge height. This implies that overcompensated smaller voids are embedded in very high density regions, unlike their subcompensated counterpart, thus indicating two possibly different processes for small voids formation. Larger voids exhibit lower ridges as outer radial layers also includes all sort of structures, thus being the difference between large overcompensated and subcompensated voids less conclusive.

All the previous results hold for both finding schemes, thereby pointing out to an universal radial profile of voids (subcompensated and overcompensated), and not only for the internal structure (Colberg et al. 2005; Ricciardelli et al. 2013), but also for outer regions (Lavaux & Wandelt 2012; Hamaus et al. 2014).

5.3.2 *Velocity profiles*

Additionally, in middle panels of Fig. 4 we calculate radial projected velocity profiles, where positive values implies outflow of matter, while negative ones indicates infall flows, all from the void centre.

A general feature of subcompensated voids is outward velocity profiles, indicating that matter all along these voids and their outsides is being pulled out. On the other hand, overcompensated voids exhibit an initial outward profile, as expected from a low density region. However, approximately at the radius of the compensation ridge, the velocity becomes negative, thus indicating an infall flow of matter further than the compensation ridge. This shows that the high density structures associated to a compensation ridge

indeed dominate the matter flow from inside the void as well as falling flows from outsides.

5.3.3 *FA profiles*

6 CONCLUSIONS

REFERENCES

Abazajian K., et al. (the SDSS Collaboration) 2003, AJ, 126, 2081
Basser P., 1995, NMR in Biomedical Imaging, 8, 333
Bertschinger E., 1985, ApJS, 58, 1
Beucher S., Lantuejoul C., 1979, in Proceedings International Workshop on Image Processing, CCETT/IRISA, Rennes, France
Beucher S., Meyer F., 1993, Mathematical Morphology in Image Processing. Marcel Deker, New York
Blumenthal G. R., da Costa L. N., Goldwirth D. S., Lecar M., Piran T., 1992, ApJ, 388, 234
Bond J. R., Kofman L., Pogosyan D., 1996, Nature, 380, 603
Brunino R., Trujillo I., Pearce F. R., Thomas P. A., 2007, MNRAS, 375, 184
Ceccarelli L., Padilla N. D., Valotto C., Lambas D. G., 2006, MNRAS, 373, 1440
Ceccarelli L., Paz D., Lares M., Padilla N., Lambas D. G., 2013, MNRAS, 434, 1435
Chincarini G., Rood H. J., 1975, Nature, 257, 294
Colberg J. M., Pearce F., et al. 2008, MNRAS, 387, 933
Colberg J. M., Sheth R. K., Diaferio A., Gao L., Yoshida N., 2005, MNRAS, 360, 216
Colless M., et al. (the 2dFGRS Team), 2001, MNRAS, 328, 1039
Colless M., et al. (the 2dFGRS Team), 2003, VizieR Online Data Catalog, 7226
Croton D. J., et al. 2004, MNRAS, 352, 828
Dubinski J., da Costa L. N., Goldwirth D. S., Lecar M., Piran T., 1993, ApJ, 410, 458
Einasto J., Joeveer M., Saar E., 1980a, MNRAS, 193, 353
Einasto J., Joeveer M., Saar E., 1980b, Nature, 283, 47
Forero-Romero J. E., Contreras S., Padilla N., 2014, MNRAS, 443, 1090
Forero-Romero J. E., Hoffman Y., Gottlöber S., Klypin A., Yepes G., 2009, MNRAS, 396, 1815
Foster C., Nelson L. A., 2009, ApJ, 699, 1252
Gottlöber S., Łokas E. L., Klypin A., Hoffman Y., 2003, MNRAS, 344, 715
Gregory S. A., Thompson L. A., 1978, ApJ, 222, 784
Hahn O., Porciani C., Carollo C. M., Dekel A., 2007, MNRAS, 375, 489
Hamaus N., Sutter P. M., Wandelt B. D., 2014, ArXiv e-prints
Hoffman Y., Metuki O., Yepes G., Gottlöber S., Forero-Romero J. E., Libeskind N. I., Knebe A., 2012, MNRAS, 425, 2049
Hoffman Y., Shaham J., 1982, ApJL, 262, L23
Hoyle F., Vogeley M. S., 2004, ApJ, 607, 751
Icke V., 1984, MNRAS, 206, 1P
Jarosik N., Bennett C. L., et al. 2011, ApJS, 192, 14
Kauffmann G., Fairall A. P., 1991, MNRAS, 248, 313

Kirshner R. P., Oemler Jr. A., Schechter P. L., Shectman S. A., 1981, ApJL, 248, L57

Kirshner R. P., Oemler Jr. A., Schechter P. L., Shectman S. A., 1987, ApJ, 314, 493

Klypin A. A., Trujillo-Gomez S., Primack J., 2011, ApJ, 740, 102

Lavaux G., Wandelt B. D., 2012, ApJ, 754, 109

Libeskind N. I., Hoffman Y., Forero-Romero J., Gottlöber S., Knebe A., Steinmetz M., Klypin A., 2013, MNRAS, 428, 2489

Martel H., Wasserman I., 1990, ApJ, 348, 1

Micheletti D., et al. 2014, ArXiv e-prints

Muñoz-Cuartas J. C., Müller V., Forero-Romero J. E., 2011, MNRAS, 417, 1303

Müller V., Arbabi-Bidgoli S., Einasto J., Tucker D., 2000, MNRAS, 318, 280

Nadathur S., Hotchkiss S., 2014, MNRAS, 440, 1248

Nasonova O. G., Karachentsev I. D., 2011, Astrophysics, 54, 1

Neyrinck M. C., 2008, MNRAS, 386, 2101

Neyrinck M. C., Falck B. L., Szalay A. S., 2013, ArXiv e-prints

Pan D. C., Vogeley M. S., Hoyle F., Choi Y.-Y., Park C., 2012, MNRAS, 421, 926

Patiri S. G., Betancort-Rijo J., Prada F., 2006, MNRAS, 368, 1132

Patiri S. G., Prada F., Holtzman J., Klypin A., Betancort-Rijo J., 2006, MNRAS, 372, 1710

Platen E., van de Weygaert R., Jones B. J. T., 2007, MN-RAS, 380, 551

Plionis M., Basilakos S., 2002, MNRAS, 330, 399

Regos E., Geller M. J., 1991, ApJ, 377, 14

Ricciardelli E., Quilis V., Planelles S., 2013, MNRAS, 434, 1192

Riebe K., Partl A. M., Enke H., Forero-Romero J., Gottloeber S., Klypin A., Lemson G., Prada F., Primack J. R., Steinmetz M., Turchaninov V., 2013, Astronomische Nachrichten, 334, 691

Rojas R. R., Vogeley M. S., Hoyle F., Brinkmann J., 2005, ApJ, 624, 571

Schaap W. E., van de Weygaert R., 2000, A&A, 363, L29

Shandarin S., Feldman H. A., Heitmann K., Habib S., 2006, MNRAS, 367, 1629

Sheth R. K., van de Weygaert R., 2004, MNRAS, 350, 517

Sutter P. M., Lavaux G., Hamaus N., Pisani A., Wandelt B. D., Warren M. S., Villaescusa-Navarro F., Zivick P., Mao Q., Thompson B. B., 2014, ArXiv e-prints

Sutter P. M., Lavaux G., Wandelt B. D., Weinberg D. H., 2012, ApJ, 761, 44

Sutter P. M., Lavaux G., Wandelt B. D., Weinberg D. H., Warren M. S., 2014, MNRAS, 438, 3177

Tikhonov A. V., 2006, Astronomy Letters, 32, 727

Tikhonov A. V., 2007, Astronomy Letters, 33, 499

van de Weygaert R., van Kampen E., 1993, MNRAS, 263, 481

von Benda-Beckmann A. M., Müller V., 2008, MNRAS, 384, 1189

York D. G., et al. (the SDSS Collaboration), 2000, AJ, 120, 1579

Zeldovich I. B., Einasto J., Shandarin S. F., 1982, Nature, 300, 407

Zel'dovich Y. B., 1970, A&A, 5, 84